Available online at www.sciencedirect.com
ScienceDirect
Trans. Nonferrous Met. Soc. China 32(2022) 3516−3533
Transactions of Nonferrous Metals Society of China
www.tnmsc.cn

Effect of solution treatment time on plasticity and ductile fracture of 7075 aluminum alloy sheet in hot stamping process

Hui-cheng GENG[1], Yi-lin WANG[1], Bin ZHU[1], Zi-jian WANG[2], Yi-sheng ZHANG[1]

1. State Key Lab of Materials Processing and Die and Mould Technology, Huazhong University of Science and Technology, Wuhan 430074, China;
2. School of Iron and Steel, Soochow University, Suzhou 215006, China

Received 4 September 2021; accepted 20 April 2022

Abstract: The effect of solution treatment time on the post-formed plasticity and ductile fracture of 7075 aluminum alloy in the hot stamping process was studied. Tensile tests were conducted on the specimens subjected to the hot stamping process with different solution treatment time. The digital image correlation (DIC) analysis was used to obtain the strain of the specimen. Based on the experiments and modeling, the Yld2000-3d yield criterion and the DF2014 ductile fracture criterion were calibrated and used to characterize the anisotropy and fracture behavior of the metal, respectively. Furthermore, the microstructure of specimens was studied. The experimental and simulation results indicate that the 7075 aluminum alloy retains distinct anisotropy after the hot stamping process, and there is no obvious effect of extending the solution treatment time on the material anisotropy. However, it is found that a longer solution treatment time can increase the fracture strain of the aluminum alloy during the hot stamping process, which may be related to the decrease of the second-phase particles size.
Key words: 7075 aluminum alloy; hot stamping; solution treatment time; anisotropy; ductile fracture

1 Introduction

During the hot stamping process of high-strength aluminum alloy, the alloy sheet is first heated to the solution treatment temperature and kept for a period of time, then the sheet is formed and quenched in a mold, and the artificial ageing treatment is applied to the parts in the end to achieve good performance [1−3]. The hot stamping process can be used to form high-strength complex-shaped parts for it can improve the formability of sheet metal effectively [4,5]. Many studies have been conducted on the forming process during hot stamping, such as the stress and strain state, friction behavior, and formability of sheet metal during forming [6,7], but there were rare studies on the post-formed properties of parts. It is meaningful to study the post-formed performance of the parts for the design of lightweight structures and the modeling of vehicle collision [8]. Thus, this work was focused on the plasticity and ductile fracture of the 7075 aluminum alloy subjected to the hot stamping process and the effect of process parameters on the final mechanical properties of the material was explored.

In the hot stamping process, the solution treatment can promote the recrystallization of the crystal grains, which will affect the material anisotropy [9,10]. Some studies have been conducted on the plasticity of aluminum alloy sheets subjected to the hot stamping process. OMER et al [11] have studied the constitutive behavior of AA7075 and a developmental 7000-series alloy subjected to hot forming and found that after the solution treatment of 470 °C,

Corresponding author: Yi-lin WANG, Tel: +86-13995566259, E-mail: wangyilin@hust.edu.cn
DOI: 10.1016/S1003-6326(22)66036-9

7 min, the materials showed significant anisotropy. GARRETT et al [12] found that with the extension of the solution treatment time, the difference of the max flow stress in different directions was minimized, and 20 min was needed to eliminate the material anisotropy in terms of the flow stress in different directions. CHOI et al [13] have conducted a comparison on the anisotropy behavior of 7075 aluminum alloy under T6 temper and W temper (470 °C, 15 min solution treatment + water quenching) and found that the Lankford coefficient and normalized yield stress had little difference between the two conditions. These studies proved that the solution treatment has a certain effect on the plasticity of aluminum alloy sheets during hot stamping. However, the relationship between the change of material anisotropy and the solution treatment is not clear, and especially, the study on the effect of solution treatment on the *r*-value is lacking. It is necessary to discuss the effect of solution treatment on the plastic anisotropy of aluminum alloy subjected to the hot stamping process in detail.

It is generally believed that the ductile fracture of sheet metals is associated with the nucleation, growth, and coalescence of micro-voids [14−16]. For aluminum alloys, the micro-voids can nucleate at the second-phase particles or inclusions [17,18]. Increasing the solution treatment temperature and time within a certain range, or adopting the stepped solution treatment, can reduce the second-phase particle volume fraction, which has a great influence on the ductile fracture of aluminum alloy [19−21]. However, for the hot stamping process of aluminum alloy, the solution treatment time is relatively short, and the aluminum alloy sheet used is usually in the T6 temper [22,23]. Therefore, the initial state of blanks and process parameters for solution treatment in hot stamping is somewhat different from those in the general solution treatment process. Considering this, probing into the influence of the solution treatment during hot stamping on the dissolution of the second-phase particles, and analyzing its effects on the fracture behavior of the material, is of great significance for formulating appropriate process parameters for the hot stamping process.

In this work, based on the hot stamping process, the plasticity and ductile fracture of 7075 aluminum alloy with different solution treatment time were studied. The hot stamping process with different solution treatment time was applied to the 7075-T6 aluminum alloy sheets. A series of specimens with various geometries and orientations were extracted from the sheets, and tensile tests were conducted. The Yld2000-3d anisotropic yield function and the DF2014 ductile fracture criterion were calibrated and used for anisotropy and fracture characteristics description, respectively. Meanwhile, the microstructure of 7075 aluminum alloy with different solution treatment time was studied to clarify the relationship among solution treatment time, microstructure, and material properties.

2 Experimental

2.1 Material and treatment

The high-strength heat-treatable 7075-T6 Al alloy sheet with a nominal thickness of 1.5 mm was used in this work. The chemical compositions of the sheet metal are listed in Table 1.

Table 1 Chemical compositions of 7075-T6 aluminum alloy (wt.%)

Mg	Zn	Mn	Cu	Fe	Cr	Si	Al
3.161	5.895	0.1778	1.63	0.1309	0.2113	0.03	Bal.

Rectangular sheets (260 mm×170 mm) were machined parallel to the rolling direction. Then, the sheets were subjected to the process shown in Fig. 1, which consisted of the following steps: (1) solution treatment performed at 480 °C and kept for different time; (2) quickly transferring the hot sheet to the cold flat mold (keeping room temperature) for quenching; (3) artificial ageing at 120 °C for 24 h and finally cooled in air. In Step (1), the hot air furnace was employed for solution treatment of the aluminum alloy sheets, as the hot air in the furnace can raise the sheet temperature to 480 °C in a short time (about 6 min) and the heating-up stage has little effect on the metal properties. After the sheet temperature reached 480 °C, different holding time was applied to the sheets: 0, 10, 20, and 30 min, and to make it easier to describe these different process conditions, they were named SST0, SST10, SST20, and SST30, respectively. Different treatment conditions in this work are listed in Table 2. The heating curve of the 7075 aluminum alloy sheet in hot air furnace was recorded by the thermocouples and presented as the inset in Fig. 1.

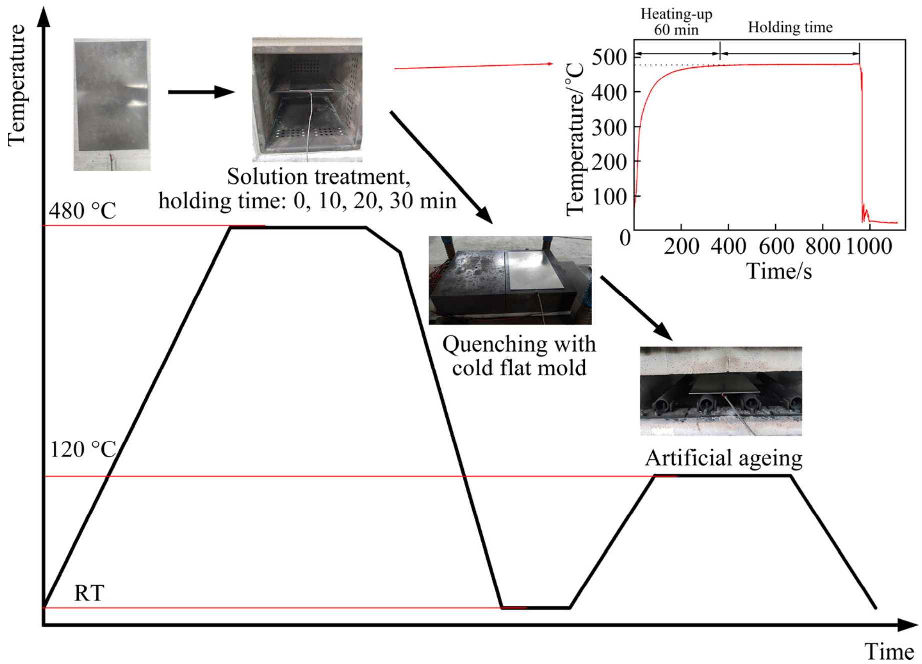

Fig. 1 Schematic diagram of experimental process for 7075-T6 aluminum alloy sheets

Table 2 Different treatment conditions for 7075-T6 aluminum alloy sheets

Treatment	Solution treatment			Quenching	Artificial ageing	
	Temperature/°C	Heating-up time/min	Holding time/min		Temperature/°C	Time/h
SST0	480	6	0	By cold flat mold	120	24
SST10	480	6	10	By cold flat mold	120	24
SST20	480	6	20	By cold flat mold	120	24
SST30	480	6	30	By cold flat mold	120	24

For each of the four 7075 aluminum alloy sheets with different solution treatment time, the same experiments were conducted. A series of plasticity and fracture specimens were extracted from these metal sheets, and the Shimadzu tensile testing machine (AG−IC 100 kN) was used for mechanical performance testing. The tensile tests were conducted under displacement control with an initial strain rate of 0.001 s^{-1}, which was regarded as a quasi-static condition. The uniform speckle pattern was sprayed on the specimen surface, and the digital image correlation (DIC) analysis was used to obtain the surface strain and the elongation of the specimens during testing.

2.2 Plasticity experiments

To accurately describe the anisotropy of the sheet metal with different solution treatment time, specimens with different geometries and orientations were machined: (1) uniaxial tension specimens along the rolling direction (0°), diagonal direction (45°), and transverse direction (90°); (2) plane-strain tension specimen along the rolling direction, and (3) disc compression specimen. The geometries of the specimens for plasticity characterization are shown in Fig. 2.

The uniaxial tension tests were conducted with a crosshead velocity of 2.28 mm/min. For specimens with different solution treatment time, the corresponding true stress−true strain curves are shown in Figs. 3(a−d). It can be seen that the solution treatment time has little effect on the flow stress, and with the same solution treatment time, the directional dependence in the flow stresses (i.e., anisotropy in flow stress) is visible. The anisotropy of flow stress was quantified by normalizing the flow stress $\hat{\sigma}_{45}=\sigma_{45}/\sigma_0$ and $\hat{\sigma}_{90}=\sigma_{90}/\sigma_0$, over the accumulated plastic work, as shown in Figs. 3(e−h). The r-value, defined as $r=\mathrm{d}\varepsilon_{\mathrm{w}}^{\mathrm{p}}/\mathrm{d}\varepsilon_{\mathrm{t}}^{\mathrm{p}}=-\mathrm{d}\varepsilon_{\mathrm{w}}^{\mathrm{p}}/(\mathrm{d}\varepsilon_{\mathrm{l}}^{\mathrm{p}}+\mathrm{d}\varepsilon_{\mathrm{w}}^{\mathrm{p}})$, was also used to characterize

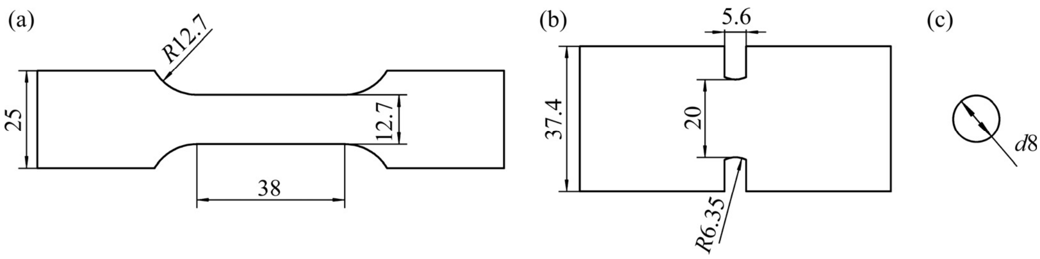

Fig. 2 Geometries of specimens for plasticity characterization: (a) Uniaxial tension specimen; (b) Plane-strain tension specimen; (c) Disc compression specimen (Unit: mm)

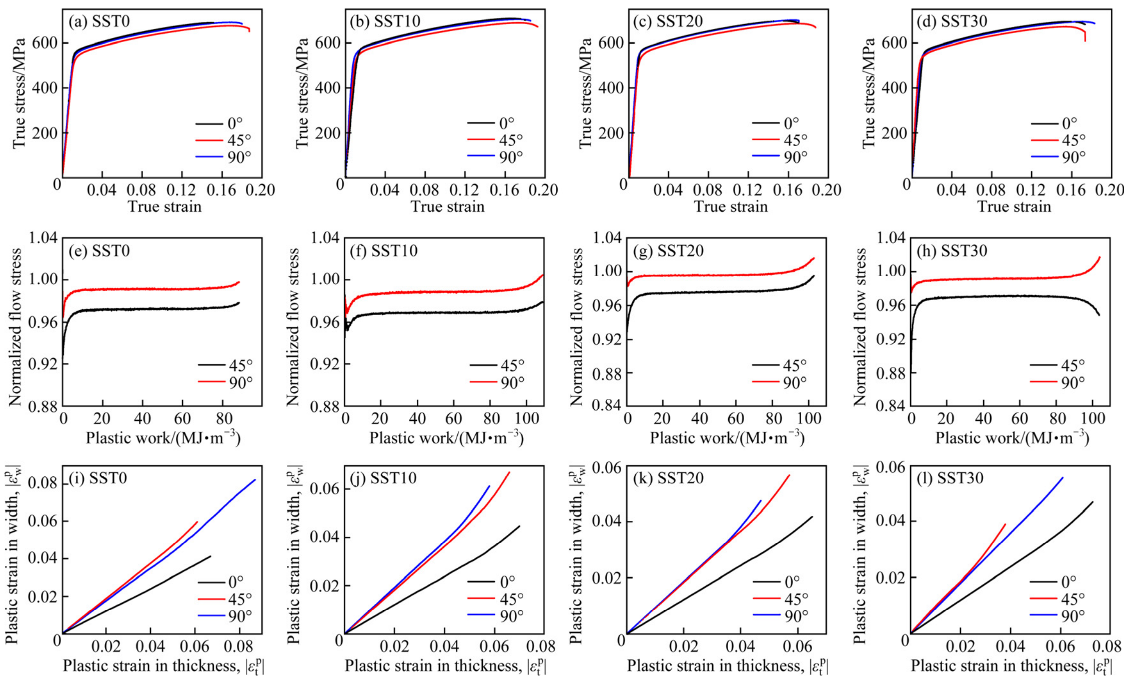

Fig. 3 Experimental results of uniaxial tension specimens under different treatment conditions: (a−d) True stress−true stain curves; (e−h) Normalized flow stress; (i−l) Relationship between plastic strain in width and thickness

the plastic anisotropy. The axial plastic strain $\varepsilon_{\mathrm{l}}^{\mathrm{p}}$ and the width plastic strain $\varepsilon_{\mathrm{w}}^{\mathrm{p}}$ were extracted using the 30 mm- and 10 mm-long virtual DIC extensometers on the surface of the specimens, respectively. The relationship between the plastic strain in width and in thickness are shown in Figs. 3(i−l). It is found that before necking, the slope of the relationship curves remained constant.

The shape of the plane-strain tension specimen restricts the deformation of the test area during stretching and makes the central area of the specimen reach a plane strain state. But the edge of the test area is still in a uniaxial tension state. As a result, the stress state and strain state along the cross-section of the test area are nonuniform. However, the axial true stress−true stain curve under plane strain state is a demand for plasticity characterization. To solve the problem, the method proposed by DICK was adopted [24]. Combining the experiments and the finite element modeling, the axial true stress−true strain curves at the central part of the specimens during plane-strain tension tests were obtained. The specific flowchart of the processing procedure is shown in Fig. 4.

On the one hand, the average axial stress−axial strain can be obtained by experiments, through the tensile force measured by the tensile testing machine and the surface strain measured by DIC technology. On the other hand, the material parameters obtained from uniaxial tension tests were used for the modeling of plane-strain tension tests. To simplify the simulation model, the Mises yield criterion was used. Through the simulation results, the relationship between the axial average stress $\sigma_{\mathrm{av}}^{\mathrm{ps}}$ in the cross-sectional area of the test zone and the axial true stress $\sigma_{\mathrm{l}}^{\mathrm{ps}}$ at the center of the test zone was $k_1 = \sigma_1^{ps}/\sigma_{av}^{ps} = 0.984$, and the relationship between the axial true stress σ_1^{ps} and transverse true stress σ_w^{ps} in the central point was $k_2 = \sigma_w^{ps}/\sigma_1^{ps} = 0.454$. To simplify the calculation process, it is assumed that the two factors remained unchanged during the plane-strain tension process (at least in the plastic phase). By combining the experimental average axial stress−strain results with the factor k_1, the axial true stress−true stain curves at the central point were obtained, as shown in Fig. 5. By considering factor k_2, the experimental transverse true stress at the central part could also be calculated.

The disk compression tests were performed with a crosshead velocity of 0.09 mm/min, and the displacement of the crosshead was 1 mm. After compression tests, the strain ratio between rolling and transverse direction, i.e., $r_{dc} = d\varepsilon_{90}^p/d\varepsilon_0^p = \varepsilon_{90}^p/\varepsilon_0^p$, was adopted to describe the plasticity characterization of the metal sheet. It is assumed that during the compression tests, the strain ratio of the compressed disc remained constant.

2.3 Fracture experiments

The fracture specimens were also machined along the rolling direction from the sheets with different solution treatment time, including notched-tension (NT) specimen, center-hole (CH) specimen, and shear (SS) specimen. The fracture specimen geometries are shown in Fig. 6. And during stretching, the crosshead velocity was set equal to 0.5 mm/min for the notched-tension specimens and

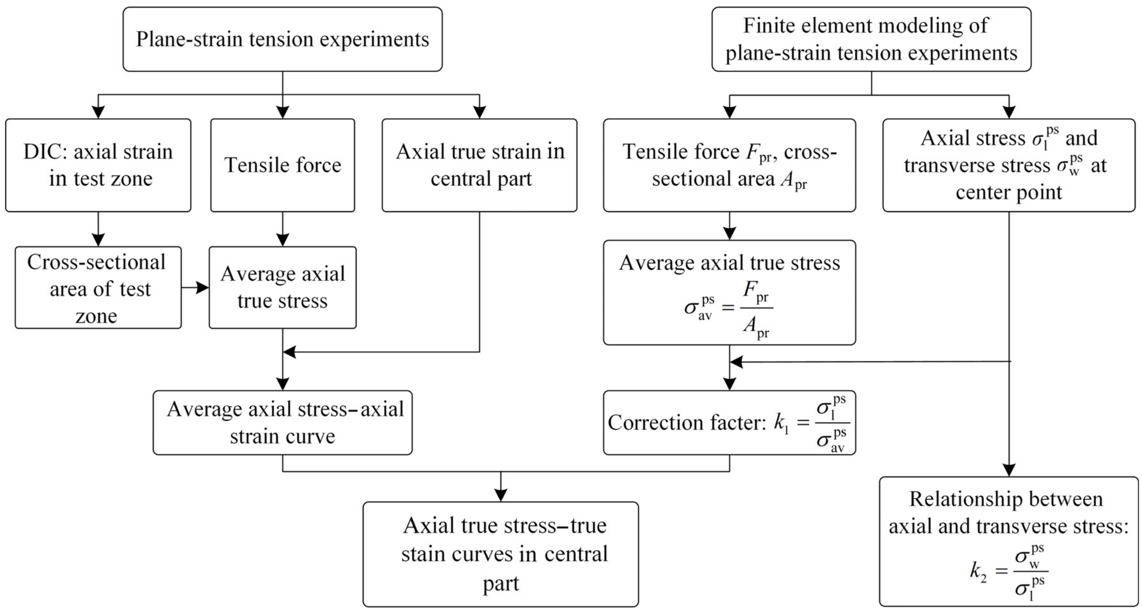

Fig. 4 Calculation procedure for axial true stress−strain curve during plain-strain tension

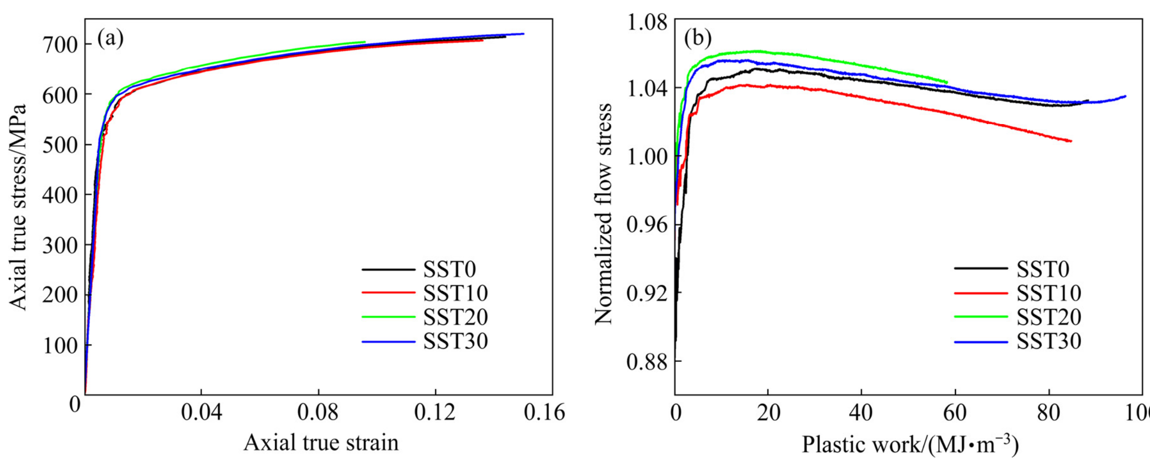

Fig. 5 Axial true stress−true strain curves (a) and normalized flow stress−plastic work curves (b) of plane-strain tension tests under different treatment conditions

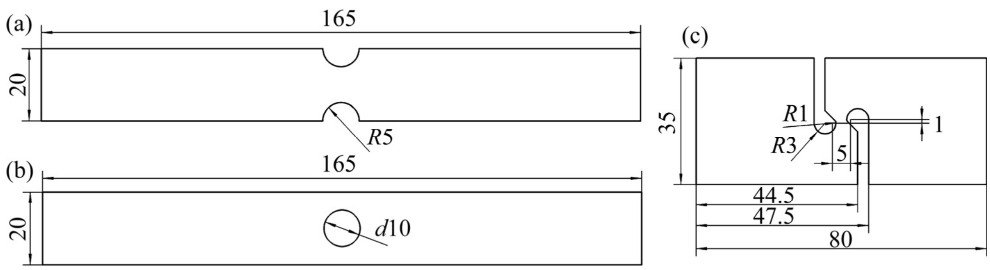

Fig. 6 Geometries of specimens for ductile fracture characterization: (a) Notched-tension specimen; (b) Center-hole specimen; (c) Shear specimen (Unit: mm)

center-hole specimens, and 0.18 mm/min for the shear specimens. Combined with the FE modeling, the fracture experiments were used for the calibration of the ductile fracture criterion.

2.4 Microstructure characterization

In this work, the relationship among solution treatment time, microstructure, and material properties was also concerned. The samples for microstructure observation were extracted from the 7075 aluminum alloy sheets after hot stamping with different solution treatment time. The size and area fraction of the second-phase particles in the matrix were studied using the scanning electron microscope (SEM, JSM−7600F).

3 Constitutive and fracture models

3.1 Anisotropic constitutive model

In this work, the anisotropic Yld2000-3d yield function proposed by DUNAND et al [25] was adopted to describe the plastic characteristics of the material. As the extended form of the Yld2000-2d yield function [26], the Yld2000-3d function was used for the description of three-dimensional stress states and can be expressed as

$$\phi=\phi'(\boldsymbol{X}')+\phi''(\boldsymbol{X}'')=2\bar{\sigma}^{a} \tag{1}$$

with

$$\phi'(\boldsymbol{X}')=\left[\left(X'_{11}-X'_{22}\right)^2+4\left(X'^2_{12}+X'^2_{13}+X'^2_{23}\right)\right]^{\frac{a}{2}} \tag{2}$$

$$\phi''(\boldsymbol{X}'')=\left[\frac{3}{2}\left(X''_{11}+X''_{22}\right)+\frac{1}{2}\sqrt{\left(X''_{11}-X''_{22}\right)^2+4\left(X''^2_{12}+X''^2_{13}+X''^2_{23}\right)}\right]^{a}+\left[\frac{3}{2}\left(X''_{11}+X''_{22}\right)-\frac{1}{2}\sqrt{\left(X''_{11}-X''_{22}\right)^2+4\left(X''^2_{12}+X''^2_{13}+X''^2_{23}\right)}\right]^{a} \tag{3}$$

where the exponent a is associated with the crystal structure of the material and a=8 is adopted for aluminum alloy (FCC material); $\bar{\sigma}$ denotes the reference yield stress. The transformed deviatoric stress vector $\boldsymbol{X}'$ and $\boldsymbol{X}''$ can be obtained with

$$\boldsymbol{X}'=\left\{X'_{11}, X'_{22}, X'_{12}, X'_{23}, X'_{13}\right\}=\boldsymbol{L}'\boldsymbol{\sigma} \tag{4}$$

$$\boldsymbol{X}''=\left\{X''_{11}, X''_{22}, X''_{12}, X''_{23}, X''_{13}\right\}=\boldsymbol{L}''\boldsymbol{\sigma} \tag{5}$$

where $\boldsymbol{\sigma}$ is the Cauchy stress vector, and the matrix $\boldsymbol{L}'$ and $\boldsymbol{L}''$ read

$$\boldsymbol{L}'=\frac{1}{3}\begin{bmatrix} 2\alpha_1 & -\alpha_1 & -\alpha_1 & 0 & 0 & 0 \\ -\alpha_2 & 2\alpha_2 & -\alpha_2 & 0 & 0 & 0 \\ 0 & 0 & 0 & 3\alpha_7 & 0 & 0 \\ 0 & 0 & 0 & 0 & 3\alpha_9 & 0 \\ 0 & 0 & 0 & 0 & 0 & 3\alpha_{10} \end{bmatrix} \tag{6}$$

$$\boldsymbol{L}''=\frac{1}{9}\begin{bmatrix} -2\alpha_3+2\alpha_4+8\alpha_5-2\alpha_6 & \alpha_3-4\alpha_4-4\alpha_5+4\alpha_6 & \alpha_3+2\alpha_4-4\alpha_5-2\alpha_6 & 0 & 0 & 0 \\ 4\alpha_3-4\alpha_4-4\alpha_5+\alpha_6 & -2\alpha_3+8\alpha_4+2\alpha_5-2\alpha_6 & -2\alpha_3-4\alpha_4+2\alpha_5+\alpha_6 & 0 & 0 & 0 \\ 0 & 0 & 0 & 9\alpha_8 & 0 & 0 \\ 0 & 0 & 0 & 0 & 9\alpha_{11} & 0 \\ 0 & 0 & 0 & 0 & 0 & 9\alpha_{12} \end{bmatrix} \tag{7}$$

Finally, the anisotropy of the 7075 aluminum alloy sheets with different solution treatment time can be described through the Yld2000-3d anisotropic yield function with the 12 material constants α_i, i=1, 2, ⋯, 12. As DUNAND et al [25] put forward in their study, α_9=α_{10}=α_{11}=α_{12}=1 was set in the model.

The results of the plasticity experiments were used for the identification of the anisotropy parameters: (1) for the uniaxial tension tests along different directions, the yield stress ratios ($\hat{\sigma}_\theta$, θ=0°, 45°, 90°) and r-values (r_θ, θ=0°, 45°, 90°) at plastic work of 20 MJ/m^3, (2) for the plane-strain tension tests, the axial normalized stress σ_{ps} and the ratio between the axial stress and transverse stress in the central point, and (3) for the disk compression tests, the strain ratio between rolling and transverse direction (r_{dc}). Corresponding plastic parameters are given in Table 3. These parameters were used for solving the yield function coefficients, and an error function was established [27]:

$$\varepsilon(\alpha_1,\ \cdots,\ \alpha_8)=\omega_Y\cdot\sum_{i=1}^{3}\left(\frac{\bar{\sigma}_\theta-Y_{\rm ref}}{Y_{\rm ref}}\right)^2+\omega_Y\cdot\left(\frac{\bar{\sigma}_{\rm ps}-Y_{\rm ref}}{Y_{\rm ref}}\right)^2+\omega_r\cdot\sum_{i=1}^{3}\left(\frac{r_\theta-r_\theta^{\rm exp}}{r_\theta^{\rm exp}}\right)^2+\omega_r\cdot\left(\frac{r_{\rm dc}-r_{\rm dc}^{\rm exp}}{r_{\rm dc}^{\rm exp}}\right)^2={\rm Min} \tag{8}$$

where θ={0°, 45°, 90°}, ω_Y and ω_r are the weighting factors for the stress ratio terms and r-value terms, respectively. The objective is to minimize this error function with respect to the anisotropic parameters α_1, ⋯, α_8, and the steepest descent method was used in this work. The obtained anisotropic parameters are listed in Table 4.

The associated flow rule and the isotropic hardening assumption were adopted in the constitutive model. As the stress−strain curve of sheet metal obtained from the uniaxial tension tests usually terminated untimely due to necking, it cannot cover the strain range of the fracture experiments. It is necessary to accurately predict the post-necking hardening curve for fracture modeling. In this work, for the 7075 aluminum alloy under different treatment conditions, the isotropic Swift−Voce model was used [28]:

$$\sigma(\bar{\varepsilon}_{\rm p})=wk_{\rm s}(\bar{\varepsilon}_{\rm p}+\varepsilon_0)^{n_{\rm s}}+(1-w)\{k_{\rm v}+Q_{\rm v}[1-\exp(-\beta_{\rm v}\bar{\varepsilon}_{\rm p})]\} \tag{9}$$

where $\bar{\varepsilon}_{\rm p}$ denotes the equivalent plastic strain, $k_{\rm s}$, ε_0 and $n_{\rm s}$ are the Swift model parameters, $k_{\rm v}$, $Q_{\rm v}$ and $\beta_{\rm v}$ are the Voce model parameters, and w is the weighting factor. The notched-tension experiments were used to determine the appropriate value of w, and the finite element aided testing method [29] was used to optimize the hardening model parameters.

3.2 DF2014 ductile fracture model

The DF2014 ductile fracture model proposed by LOU et al [30] was adopted in this work, which assumed that the fracture response was independent of material orientation. However, as the Yld2000-3d yield function was used, the anisotropic plastic behavior would affect the fracture results in the modeling. The DF2014 ductile fracture model is expressed as [30]

$$\frac{1}{C_3}\int_0^{\bar{\varepsilon}_{\rm f}}\left(\frac{2}{\sqrt{L^2+3}}\right)^{C_1}\left(\left\langle\frac{f(\eta,L,C)}{f(1/3,-1,C)}\right\rangle\right)^{C_2}{\rm d}\bar{\varepsilon}=D(\bar{\varepsilon}),$$
$$\langle x\rangle=\begin{cases}x & \text{when } x\ge 0\\ 0 & \text{when } x<0\end{cases} \tag{10}$$

where η and L refer to the stress triaxiality and the Lode parameter, respectively; C represents the sensitivity of the fracture cut-off value for the stress triaxiality to microstructure; C_1, C_2, and C_3 are material constants; $\bar{\varepsilon}_{\rm f}$ denotes the equivalent

Table 3 Material parameters of 7075 aluminum alloy under different treatment conditions

Treatment	$\hat{\sigma}_0$	$\hat{\sigma}_{45}$	$\hat{\sigma}_{90}$	σ_{ps}	r_0	r_{45}	r_{90}	r_{dc}
SST0	1	0.972	0.991	1.0498	0.5997	0.9397	0.8714	0.8264
SST10	1	0.968	0.987	1.0409	0.5929	0.9056	0.9581	0.8061
SST20	1	0.974	0.995	1.0604	0.6080	0.9163	0.9296	0.8651
SST30	1	0.969	0.990	1.0539	0.5914	0.9457	0.8935	0.8973

Table 4 Yld2000-3d anisotropic coefficients for 7075 aluminum alloy under different treatment conditions

Treatment	α_0	α_2	α_3	α_4	α_5	α_6	α_7	α_8
SST0	0.9193	1.0509	1.0324	1.0162	1.0393	1.0696	0.8667	1.1704
SST10	0.9075	1.0783	1.0632	1.0194	1.0477	1.1027	0.8664	1.1666
SST20	0.9081	1.0576	1.0214	1.0067	1.0288	1.0216	0.8426	1.1896
SST30	0.9035	1.0664	1.0455	1.0173	1.0348	1.0431	0.8658	1.1818

plastic strain to fracture. This model considers the influence of the cumulative process of void nucleation, growth, and shear coalescence on fracture. it is postulated that fracture initiates as $D(\bar{\varepsilon})$ reaches unity. In the fracture model,

$$\eta=\frac{\sigma_{\mathrm{m}}}{\bar{\sigma}}=\frac{\sigma_1+\sigma_2+\sigma_3}{3\bar{\sigma}} \tag{11}$$

$$L=\frac{2\sigma_2-\sigma_1-\sigma_3}{\sigma_1-\sigma_3} \tag{12}$$

LOU et al [30] pointed out that from the microscopic point of view, the void tends to close at compressive stress, and the void closing will counteract the damage accumulation during deformation. As a result, when the stress triaxiality is small enough, a fracture is difficult to occur. Therefore, in the fracture model,

$$f(\eta,L,C)=\eta+\frac{(3-L)}{3\sqrt{L^2+3}}+C \tag{13}$$

It is adopted to determine whether a fracture occurs. The fracture will not occur if $f(\eta,L,C)\le 0$. Referring to the study of LOU et al [30], C=1/3 was taken.

3.3 Finite element modeling

At the beginning of the fracture, there is a complex 3D stress state near the fracture location, and the fracture mostly starts from inside of the specimens. It is impossible to obtain the stress state and strain state at fracture only through experiments. Thus, to solve the fracture model parameters, a method combining experiments and FE modeling was used. In this work, ABAQUS software was adopted to perform the modeling, and the user-defined subroutine UMAT was used to control the constitutive and fracture behavior of the specimens. The UMAT subroutine consisted of the Yld2000-3d yield function, the associated flow rule, the Swift−Voce hardening model, and the DF2014 fracture criterion.

As mentioned above, experiments and modeling were conducted on the notched-tension specimen, center-hole specimen, and shear specimen to solve the fracture model parameters of the material, and the corresponding simulation models were established, as shown in Fig. 7. By considering the symmetry of the specimens, the 1/2 model was adopted for the notched-tension specimen and center-hole specimen. The C3D8R elements were used and five elements were set in the thickness direction. Meanwhile, displacement loading was applied over at least 1000 time steps up to the fracture displacement measured by experiments.

4 Results and discussion

4.1 Plastic characterization

As mentioned above, the Yld2000-3d yield function was used to describe the plastic anisotropy of the 7075 aluminum alloy sheets after the hot stamping process with different solution treatment time. The yield locus under the in-plane stress condition and the projection of the yield surface on the π-plane for the material under different treatment conditions are depicted in Fig. 8. The

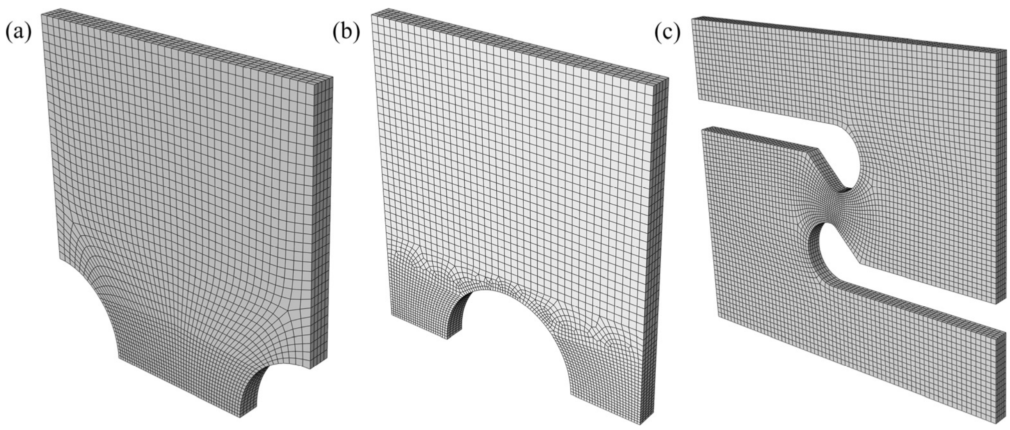

Fig. 7 Finite element meshes of fracture specimens: (a) 1/2 notched-tension specimen; (b) 1/2 center-hole specimen; (c) Shear specimen

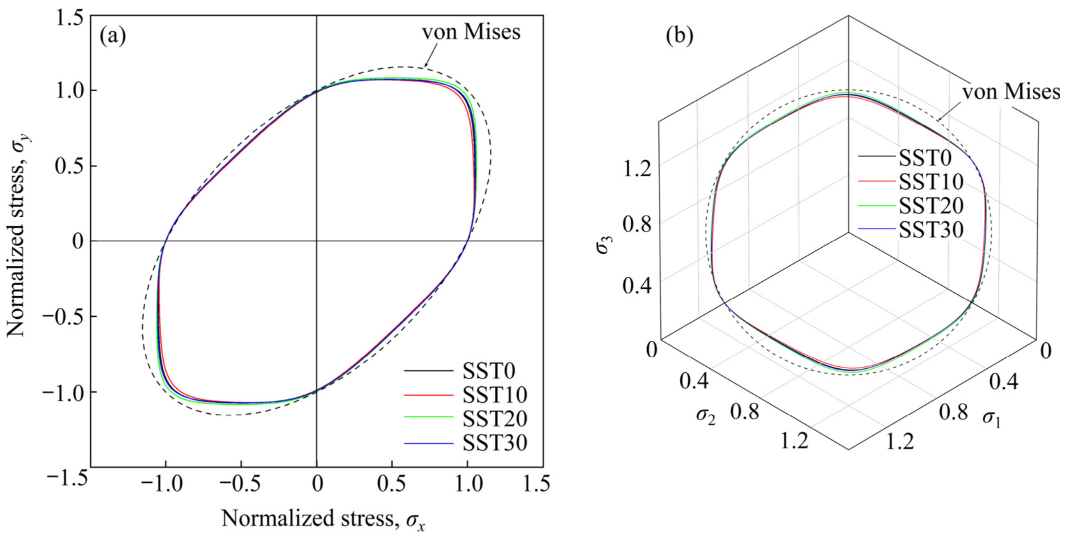

Fig. 8 Normalized shapes of yield envelopes under in-plane stress condition (a) and projection of Yld2000-3D yield function on π-plane (b) for 7075 aluminum alloy under different treatment conditions

isotropic von Mises criterion is also shown as a contrast. It is found that the shape of the obtained Yld2000-3d function has apparent differences with the von Mises function, which indicates that after the heat treatment in hot stamping, the aluminum alloy still has a certain anisotropy. The agreement of the Yld2000-3d yield loci of the material with different solution treatment time was also studied here. As the solution treatment time increases, the yield loci of the material change slightly. Even when the solution treatment time reaches 30 min, the yield locus is still similar.

The normalized yield stress and r-value acquired from Yld2000-3d and uniaxial tension tests are shown in Fig. 9. As for the normalized yield stress, it can be seen that the variation of yield stress is less than 5%, and there is little effect of solution treatment time on the normalized yield stress. However, as for the r-value, it is found that it changes significantly with the orientation, and the increase of the solution treatment time also has influences on its value. Meanwhile, it can be seen that the r-value is less than 1, which indicates that the specimen thickness reduction is stronger than the width reduction. In general, solution treatment during hot stamping has a certain effect on the yield stress and r-value of the aluminum alloy, but its effect is small.

4.2 Work-hardening

The true stress versus plastic strain curves of the 7075 aluminum alloy after the hot stamping

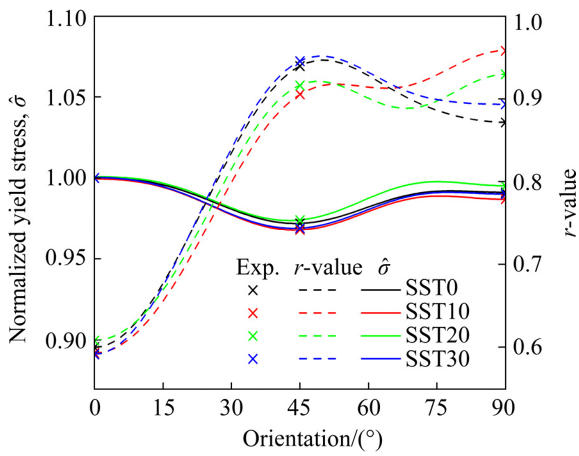

Fig. 9 Normalized yield stress and r-value predictions from Yld2000-3d vs experimental results of 7075 aluminum alloy under different treatment conditions

process with different solution treatment time are shown in Fig. 10, and the corresponding hardening model parameters of the material are listed in Table 5. It can be seen that the Swift−Voce model fits the experimental true stress−plastic strain curves well. And by comparing the force−displacement curves between notched-tension experiments and modeling, the appropriate weighting factor w between the Swift model and Voce model is determined.

4.3 Fracture characterization

The tension experiments and modeling of three specimens (notched-tension specimen, center-hole specimen, and shear specimen) were adopted to calibrate the parameters of the DF2014 fracture

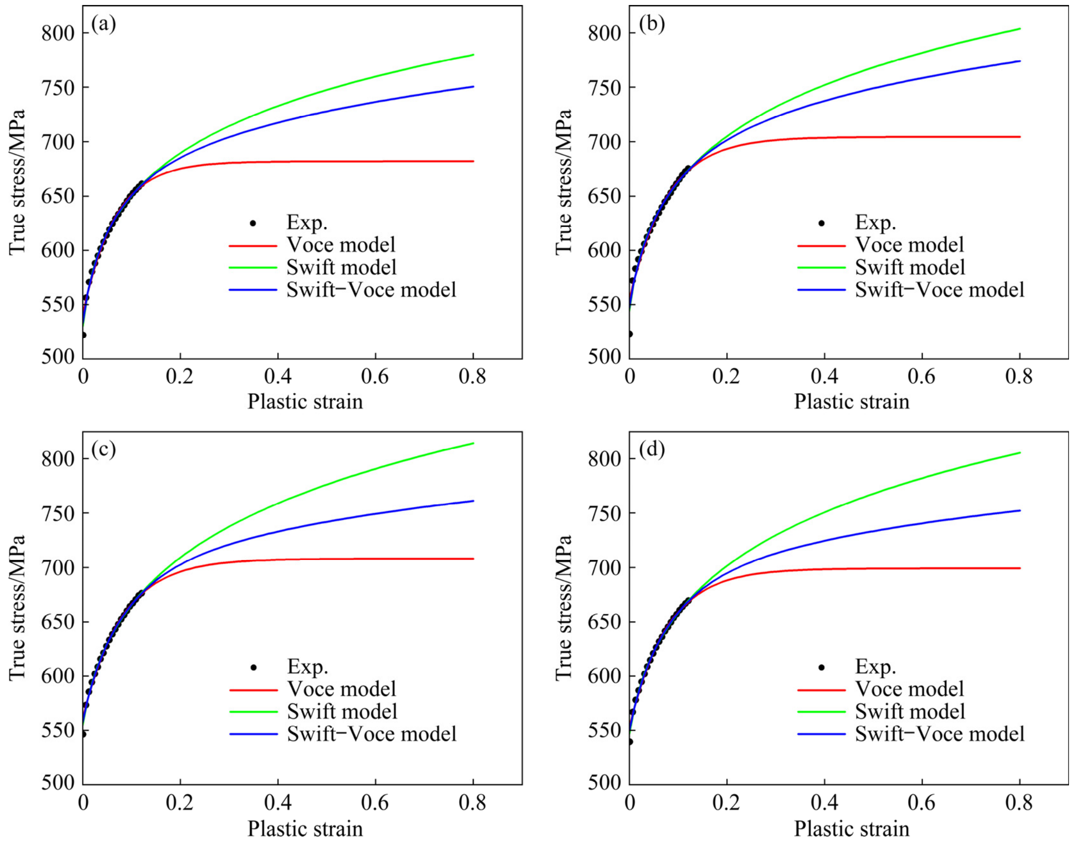

Fig. 10 Extrapolations of true stress−plastic strain curves with Swift−Voce model for 7075 aluminum alloy under different treatment conditions: (a) SST0; (b) SST10; (c) SST20; (d) SST30

Table 5 Swift−Voce model parameters of 7075 aluminum alloy under different treatment conditions

Treatment	k_s	ε_0	n_s	k_v	Q_v	β_v	w
SST0	795.0	0.01212	0.09180	540.4	141.6	15.16	0.7
SST10	820.2	0.01555	0.09871	553.3	151.2	13.05	0.7
SST20	831.5	0.02178	0.1057	560.2	147.9	12.58	0.5
SST30	822.5	0.02066	0.1052	552.5	146.8	12.92	0.5

model, and the fracture behavior of the material subjected to the hot stamping process with different solution treatment time was studied. In the fracture model, the influence of the orientation of the stress tensor was not considered, and thus, the fracture specimens were machined along the rolling direction.

It is generally believed that during stretching process, the fracture starts from the inside of the specimens, as the mid-plane of the specimens has larger stress and strain locally. It is difficult to observe the initial location for fracture through experiments, and the strain and stress states at the fracture point are also unavailable. It is necessary to combine the experiments and modeling to solve the parameters of the DF2014 fracture model.

Through modeling, it is found that the stress state of the specimens varies during stretching. As a result, the stress triaxiality and Lode parameter in the test area of the specimens are also changed, as shown in Fig. 11. The DF2014 model parameters cannot be solved analytically. Figure 11 also shows the distribution of stress triaxiality and Lode parameter in three specimens at the experimental fracture displacement. It can be seen that the stress triaxiality and Lode parameter distribution in the specimens are nonuniform, even in the middle part of the specimens.

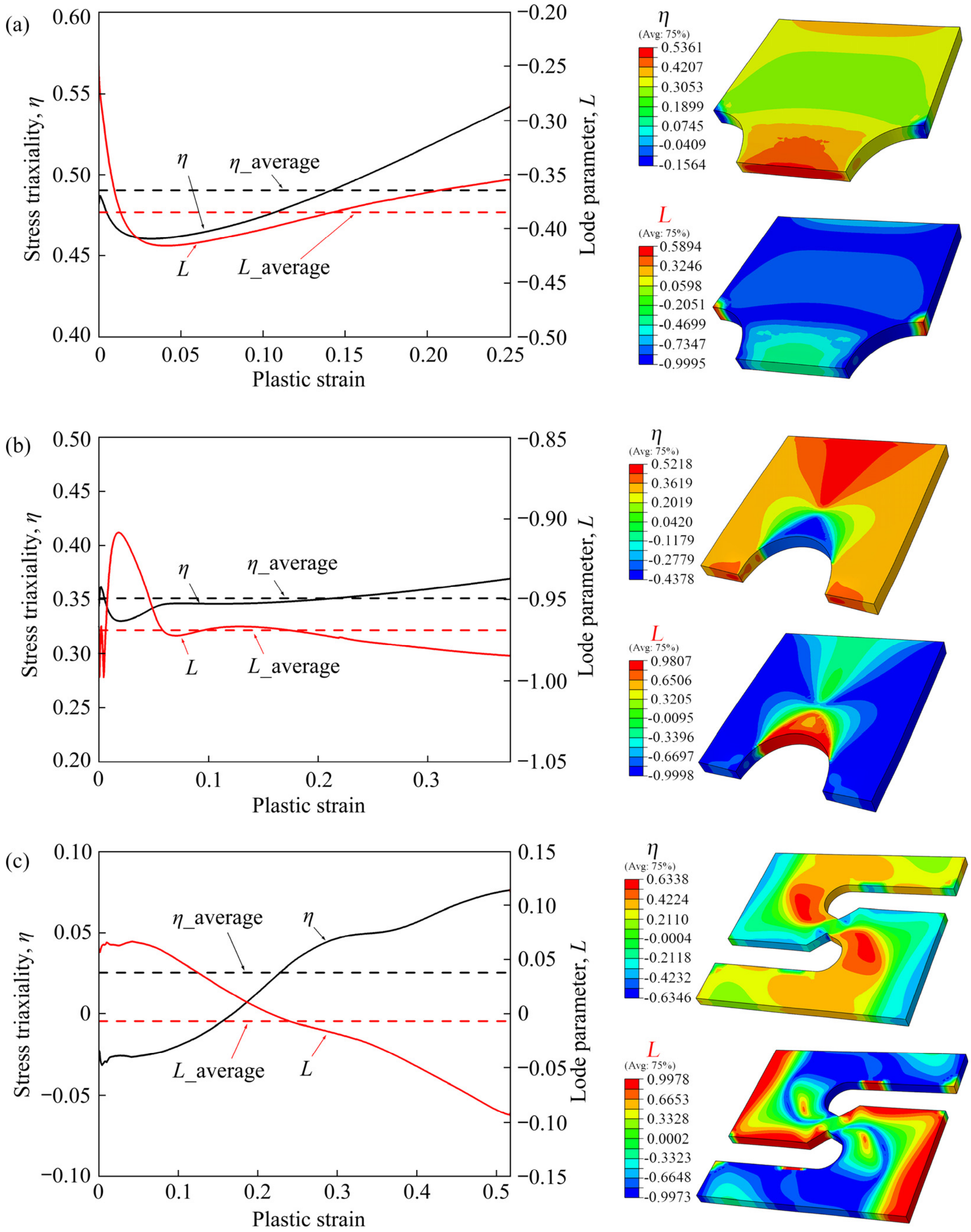

Fig. 11 Evolution of stress triaxiality and Lode parameter at center point of specimens and distribution of stress triaxiality and Lode parameter in specimens for SST0 treatment condition: (a) Notched-tension specimen; (b) Center-hole specimen; (c) Shear specimen

To acquire accurate fracture model parameters of the 7075 aluminum alloy under different treatment conditions, a series of processes were carried out, and the detailed flowchart for determining the fracture model parameters is shown in Fig. 12. First, by modeling the stretching process of three fracture specimens, the average stress triaxiality, average Lode parameter, and the plastic strain of the central element until the experimental fracture displacement were obtained, as shown in Fig. 11. These initial prediction results were used for solving the DF2014 model parameters. Then, the DF2014 model was compiled into the UMAT subroutine, which was used for modeling the fracture process of the specimens. By comparing the modeling fracture displacement d_{sim} with the

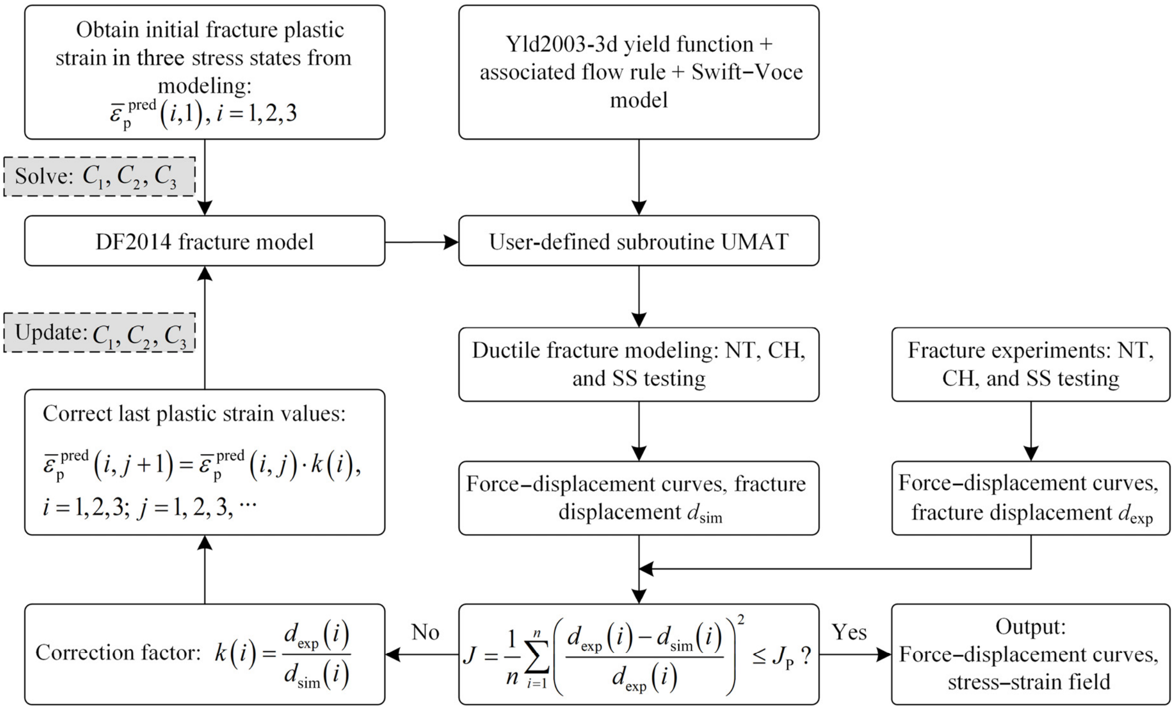

Fig. 12 Calculation procedure for determining fracture model parameters

experimental results d_{exp}, the following formula was established to measure the accuracy of the fracture model parameters [31]:

$$J=\frac{1}{n}\sum_{i=1}^{n}\left(\frac{d_{exp}(i)-d_{sim}(i)}{d_{exp}(i)}\right)^2 \tag{14}$$

where n denotes the number of fracture experiments. Set the critical value $J_P=10^{-4}$. If $J\le J_P$, it is believed that the fracture model parameters is sufficiently accurate. If $J>J_P$, the following correction factor is established:

$$k(i)=\frac{d_{exp}(i)}{d_{sim}(i)} \tag{15}$$

The factor $k(i)$ is used to improve the fracture plastic strain obtained in the last modeling. The modified fracture plastic strain is again used to calculate the DF2014 model parameters. Repeat the above processes until the DF2014 model parameters are accurate enough.

Generally, more accurate model parameters can be obtained after 4 or 5 revisions. During the revision process, the comparison between the modeling force−displacement curves and the experimental results under SST0 condition is shown in Fig. 13. It is shown that with the optimization of fracture model parameters, the fracture displacement of the specimens obtained by modeling gradually approaches the experimental result. The obtained fracture model parameters are given in Table 6.

For different treatment conditions, the comparison between the experiments and modeling force−displacement curves is shown in Fig. 14. It can be seen that the modeling force−displacement curves are in good agreement with the experimental results, and the fracture displacement prediction is accurate, which indicates that the constitutive model and fracture model parameters are appropriate. Meanwhile, it can be seen that with the extension of the solution treatment time, the fracture displacement of the specimens tends to increase.

Figure 15 shows the cloud diagram of the equivalent plastic strain of the specimens at the moment before fracturing with different solution treatment time. It is shown that the deformation is concentrated in the central part of the specimens, and the maximum plastic strain is located in the mid-plane of the specimens. By comparing the plastic strain distribution of the specimens with the same geometry under different treatment conditions, it is found that the plastic strain to fracture of the specimens becomes larger as the solution treatment time increases.

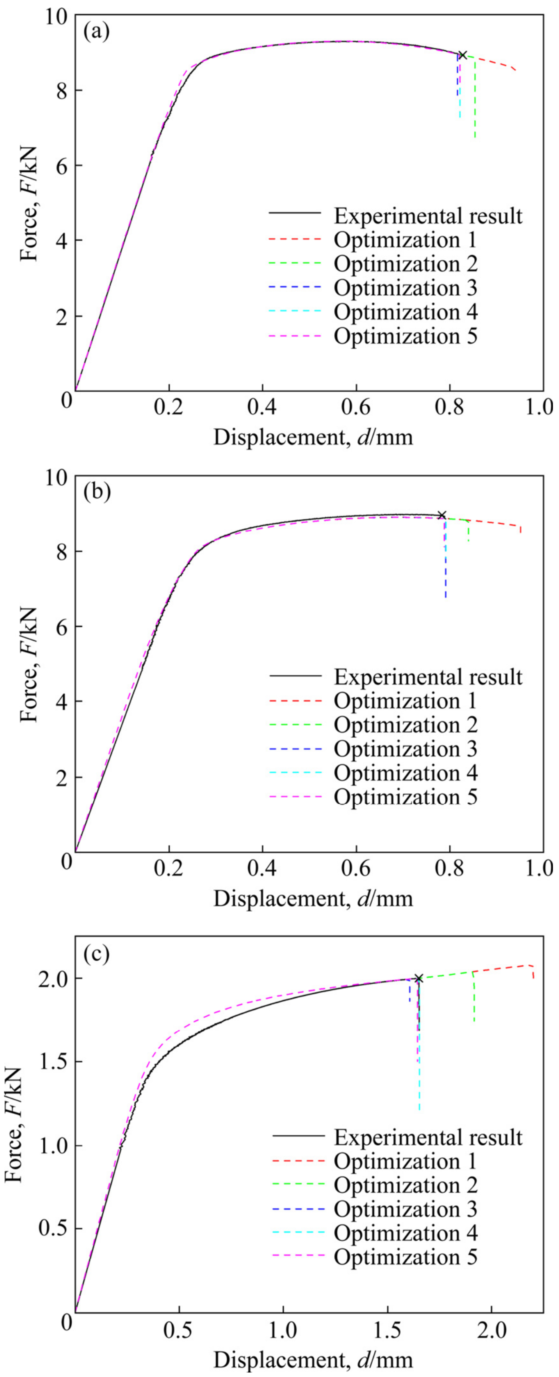

Fig. 13 Optimization process of force−displacement curves of specimens under SST0 condition: (a) Notched-tension specimen; (b) Center-hole specimen; (c) Shear specimen

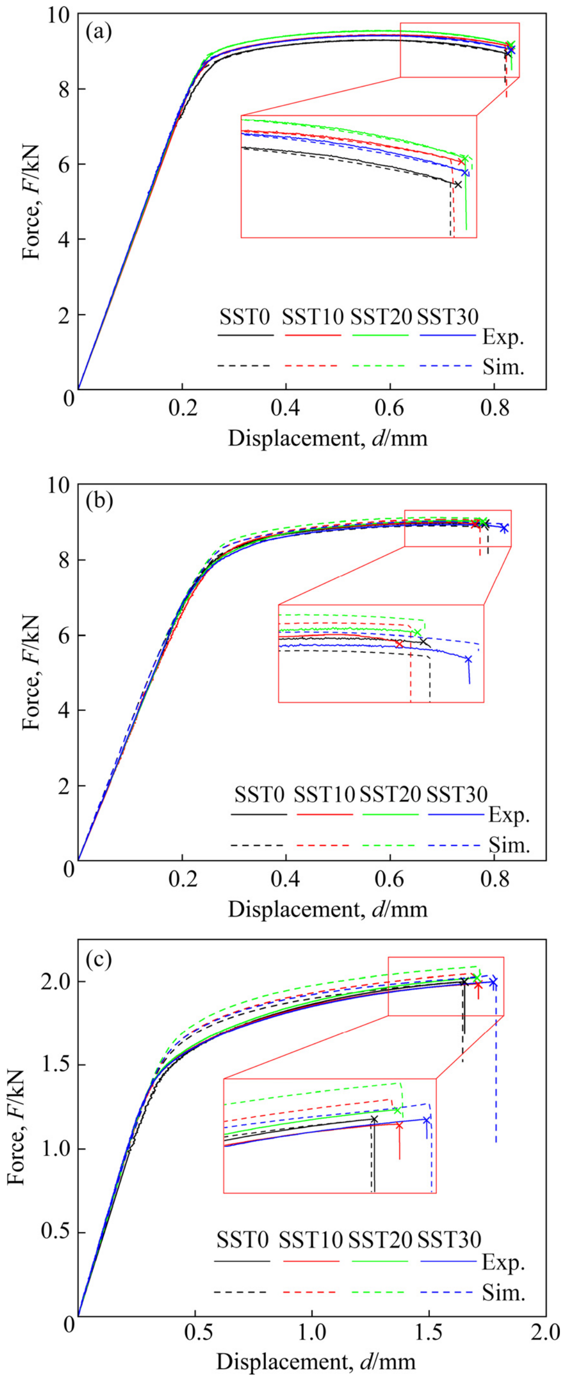

Fig. 14 Comparison of experimental and modeling force−displacement curves for specimens under different treatment conditions: (a) Notched-tension specimen; (b) Center-hole specimen; (c) Shear specimen

Table 6 Parameters of DF2014 fracture model for 7075 aluminum alloy under different treatment conditions

Treatment	C_1	C_2	C_3
SST0	1.675	1.087	0.2874
SST10	1.057	1.039	0.2697
SST20	1.363	1.124	0.2832
SST30	2.657	1.416	0.3052

Figure 16 shows distribution of accumulated damage $D(\bar{\varepsilon})$ on the specimens at the beginning of the fracture under SST0 condition. By comparing Fig. 15 and Fig. 16, it can be seen that there is a small difference between the distribution of index $D(\bar{\varepsilon})$ and the equivalent plastic strain. The distribution of the $D(\bar{\varepsilon})$ is affected by the stress state and strain state during the deformation process.

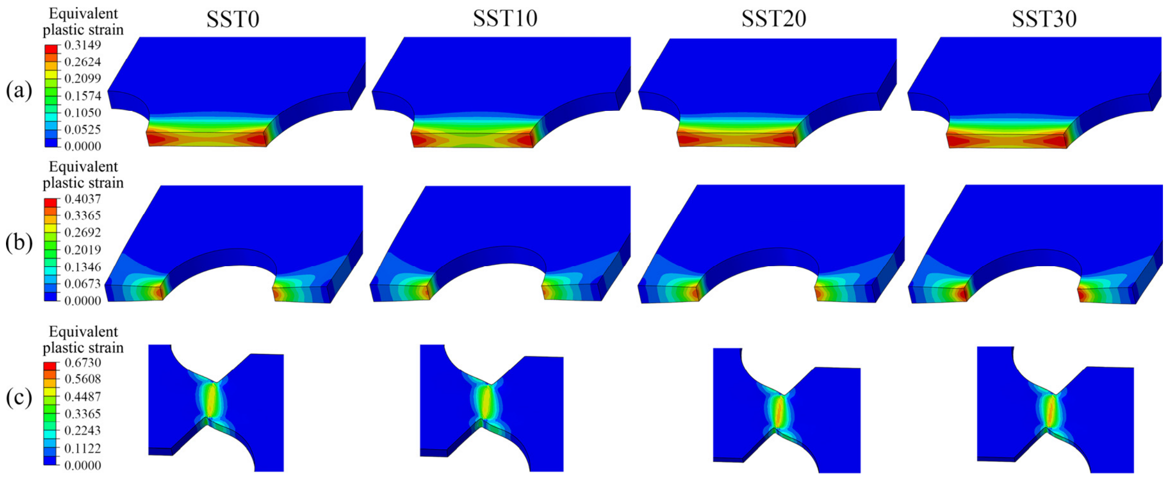

Fig. 15 Cloud diagram of equivalent plastic strain of specimens at moment before fracturing under different treatment conditions: (a) Notched-tension specimen; (b) Center-hole specimen; (c) Shear specimen

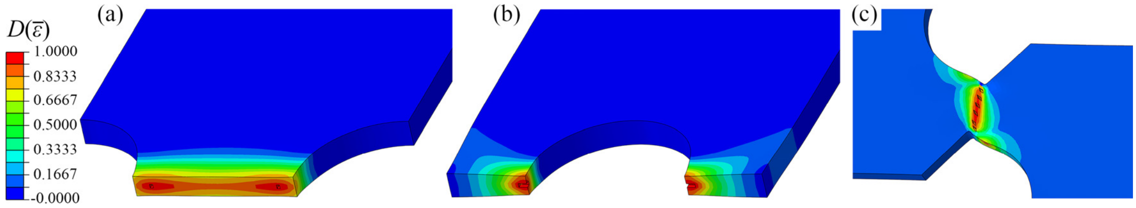

Fig. 16 Distribution of accumulated damage $D(\bar{\varepsilon})$ with fracture just occurring for specimens under SST0 condition: (a) Notched-tension specimen; (b) Center-hole specimen; (c) Shear specimen

For notched-tension specimen, it breaks first on both sides of the cross-section, which is different from what we previously predicted to break at the center of the specimen. The initial fracture positions of the specimens are near the maximum plastic strain, which is affected by the material anisotropy. This indicates that the strain distribution before fracture does have a great influence on the initial fracture location, and a suitable constitutive model during modeling is important for describing fracture characteristics.

The loading paths to fracture of the specimens with different treatment conditions are shown in Fig. 17. The loading paths were probed based on the predictions of the modeling and the required data were extracted from the location where the fracture was expected to initiate (as shown in Fig. 16). The stress triaxiality decreases in the order of notched-tension specimen, center-hole specimen, and shear specimen. And it is found that as the stress triaxiality decreases, the plastic strain to fracture increases. It is believed that with the decrease of stress triaxiality, the stress state tends to compressive stress, which will lead to the closing of the microvoids in the material, thereby increasing the fracture strain of the material. The solution treatment during the hot stamping process also affects the fracture strain of the 7075 aluminum alloy. It can be seen that for the center-hole specimen and shear specimen, the plastic strain to fracture of the specimen increases as the solution treatment time increases.

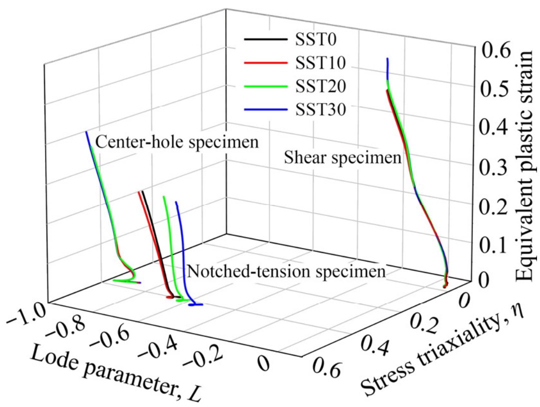

Fig. 17 Loading paths to fracture in Lode parameter and stress triaxiality space for specimens under different treatment conditions

In Fig. 18, the fracture envelopes predicted by the DF2014 model are shown in the Lode parameter and stress triaxiality space. It is shown that stress

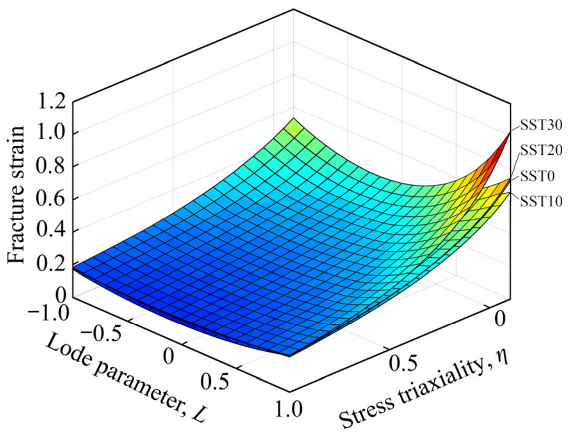

Fig. 18 Fracture envelopes of 7075 aluminum alloy under different treatment conditions predicted by DF2014 model

triaxiality has a great influence on the fracture strain. As the stress triaxiality decreases, the fracture strain of the 7075 aluminum alloy after hot stamping increases significantly. At the same time, as the Lode parameter increases, the material fracture strain first decreases and then increases. Meanwhile, the solution treatment time also affects the fracture characteristics of the alloy sheet after the hot stamping process. With the same Lode parameter and stress triaxiality, the fracture strain increases with the extension of the solution treatment time.

4.4 Microstructure characteristics

Figure 19 shows the SEM micrographs of the 7075 aluminum alloy under different treatment conditions. A large number of second-phase particles can be found in the micrographs. For different treatment conditions, the area and size of the second-phase particles (A) and the voids (B) formed by the shedding of the second-phase particles during specimen preparation were counted, and the area fraction and mean grain size of the second-phase particles in the specimens were obtained, as shown in Fig. 20. In the hot stamping process, during solution treatment, the particles in the matrix dissolve, the smaller second-phase particles disappear, and the larger particles decrease in size. Later, during the artificial ageing treatment, the undissolved second-phase particles grow up and new small particles precipitate from the matrix. As a result, for the hot stamping process of 7075

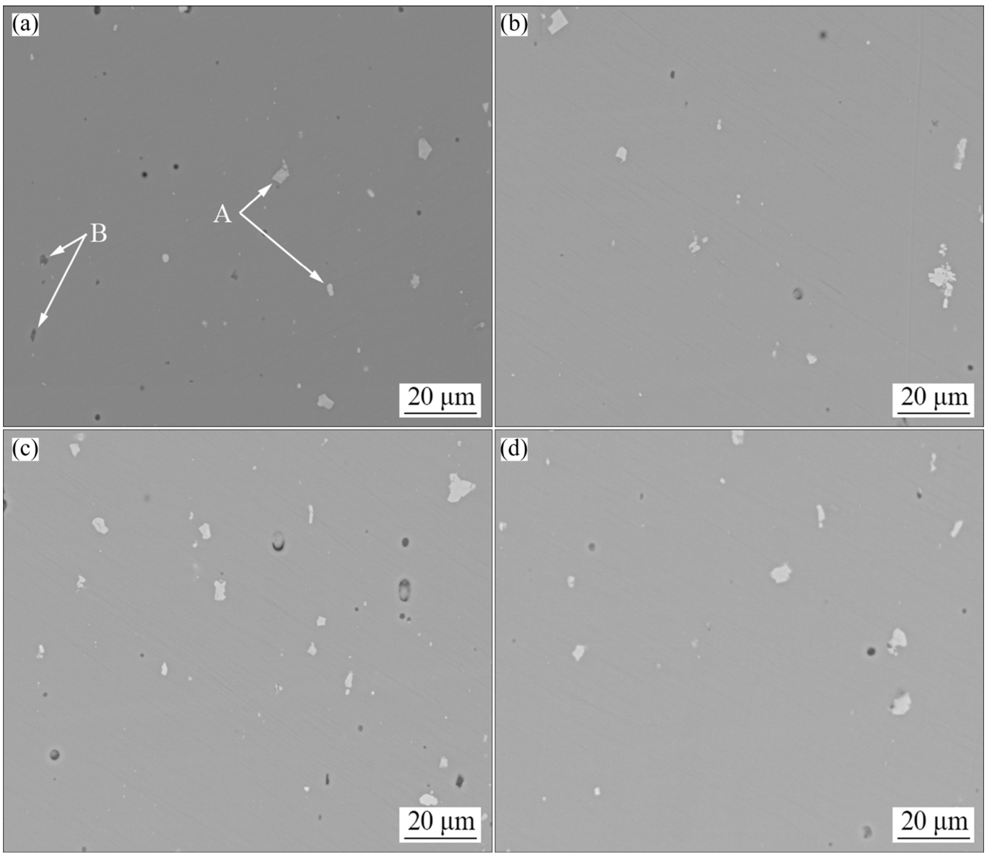

Fig. 19 SEM micrographs of 7075 aluminum alloy after hot stamping process with different solution treatment time: (a) 0 min; (b) 10 min; (c) 20 min; (d) 30 min

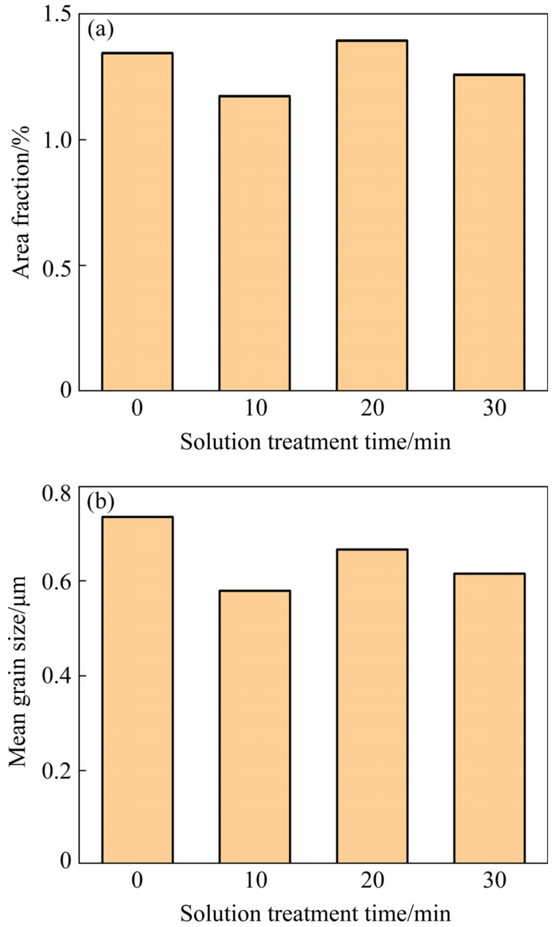

Fig. 20 Area fraction (a) and mean grain size (b) of second-phase particles in 7075 aluminum alloy after hot stamping process with different solution treatment time

aluminum alloy, the area fraction of the second-phase particles changes little with the solution treatment time, as shown in Fig. 20(a). However, the solution treatment time affects the average grain size of the second-phase particles. With the extension of the solution treatment time, the large-size particles have a longer time to dissolve and become smaller, the solute in the matrix increases and the distribution is more uniform, which is beneficial to the precipitation of more small-size particles during artificial ageing. Thus, the average size of the second-phase particles decreases as the solution treatment time increases, as shown in Fig. 20(b).

As micro-voids can nucleate at the second-phase particles when the fracture initiates, the smaller particles help reduce the possibility of void nucleation. This indicates that a longer solution treatment time can improve the fracture performance of the 7075 aluminum alloy sheet, which is consistent with the results of the fracture experiments.

5 Conclusions

(1) In the hot stamping process of aluminum alloy, solution treatment cannot eliminate the anisotropy of the sheet metal. Even after the solution treatment at 480 °C for 30 min, there is no apparent weakening of the material anisotropy.

(2) By combining experiments and modeling, and through iterative optimization, the accurate fracture strain of the specimens can be obtained, and the accuracy of the solved fracture model parameters is improved.

(3) The anisotropic behavior of the material has an impact on the predictions of the fracture strain. The anisotropic constitutive model changes the distribution of the stress and strain on the specimens during modeling.

(4) Prolonging the solution treatment time makes the average size of the second-phase particles in the material show a downward trend, which is beneficial to improving the fracture performance of the material.

(5) In the hot stamping process of aluminum alloy, a proper extension of the solution treatment time can increase the material fracture strain. However, considering the production efficiency, it is recommended to optimize the solution treatment temperature and time together or use a more efficient heating method. It is also a research direction for our later study.

Acknowledgments

The authors would like to acknowledge the State Key Lab of Materials Processing and Die and Mould Technology for their assistance in the tensile experiments and microstructure observation. This research work was funded by the National Natural Science Foundation of China (No. U1760205).

References

[1] ZHENG Kai-lun, DONG Yang-chun, ZHENG Jing-hua, FOSTER A, LIN Jian-guo, DONG Han-shan, DEAN T A. The effect of hot form quench (HFQ®) conditions on precipitation and mechanical properties of aluminium alloys [J]. Materials Science and Engineering A, 2019, 761: 138017.

[2] MA Wen-yun, WANG Bao-yu, LIN Jian-guo, TANG

Xue-feng. Influence of process parameters on properties of AA6082 in hot forming process [J]. Transactions of Nonferrous Metals Society of China, 2017, 27(11): 2454−2463.

[3] PEPPAS A, KOLLIAS K, DRAGATOGIANNIS D A, CHARITIDIS C A. Sustainability analysis of aluminium hot forming and quenching technology for lightweight vehicles manufacturing [J]. International Journal of Thermofluids, 2021, 10: 100082.

[4] WANG Ning, ILINICH A, CHEN Ming-he, LUCKEY G, D'AMOURS G. A comparison study on forming limit prediction methods for hot stamping of 7075 aluminum sheet [J]. International Journal of Mechanical Sciences, 2019, 151: 444−460.

[5] ZHANG Wen-pei, LI Huan-huan, HU Zhi-li, HUA Lin. Investigation on the deformation behavior and post-formed microstructure/properties of AA7075-T6 alloy under pre-hardened hot forming process [J]. Materials Science and Engineering A, 2020, 792: 139749.

[6] LIU Yong, ZHU Zhou-jie, WANG Zi-jian, ZHU Bin, WANG Yi-lin, ZHANG Yi-sheng. Flow and friction behaviors of 6061 aluminum alloy at elevated temperatures and hot stamping of a B-pillar [J]. The International Journal of Advanced Manufacturing Technology, 2018, 96(9/10/11/12): 4063−4083.

[7] ZHOU Jing, WANG Bao-yu, LIN Jian-guo, FU Lei, MA Wen-yu. Forming defects in aluminum alloy hot stamping of side-door impact beam [J]. Transactions of Nonferrous Metals Society of China, 2014, 24(11): 3611−3620.

[8] LUO Meng, DUNAND M, MOHR D. Experiments and modeling of anisotropic aluminum extrusions under multi-axial loading — Part II. Ductile fracture [J]. International Journal of Plasticity, 2012, 32/33: 36−58.

[9] XU D K, ROMETSCH P A, BIRBILIS N. Improved solution treatment for an as-rolled Al−Zn−Mg−Cu alloy. Part II. Microstructure and mechanical properties [J]. Materials Science and Engineering A, 2012, 534: 244−252.

[10] WANG Xiao-feng, GUO Ming-xing, PENG Wen-fei, WANG Yong-gang, ZHUANG Lin-zhong. Relationship among solution heating rate, mechanical properties, microstructure and texture of Al−Mg−Si−Cu alloy [J]. Transactions of Nonferrous Metals Society of China, 2021, 31(1): 36−52.

[11] OMER K, BUTCHER C, WORSWICK M. Characterization and application of a constitutive model for two 7000-series aluminum alloys subjected to hot forming [J]. International Journal of Mechanical Sciences, 2020, 165: 105218.

[12] GARRETT R P, LIN Jian-guo, DEAN T A. Solution heat treatment and cold die quenching in forming AA 6xxx sheet components: Feasibility study [J]. International Journal of Plasticity, 2005, 21: 1640−1657.

[13] CHOI Y, LEE J, PANICKER S S, JIN H, PANDA S K, LEE M. Mechanical properties, springback, and formability of W-temper and peak aged 7075 aluminum alloy sheets: Experiments and modeling [J]. International Journal of Mechanical Sciences, 2020, 170: 105344.

[14] ZHU Cheng-yan, WU Hao, ZHU He-guo, LI Xiang-dong, TU Chun-lei, XIE Zong-han. Mechanical properties and fracture mechanism of as-cast $MnFeCoCuNi_x$ high-entropy alloys [J]. Transactions of Nonferrous Metals Society of China, 2021, 31(1): 222−231.

[15] HA Jin-jin, BARAL M, KORKOLIS Y P. Plastic anisotropy and ductile fracture of bake-hardened AA6013 aluminum sheet [J]. International Journal of Solids and Structures, 2018, 155: 123−139.

[16] GU Gong-yao, MOHR D. Anisotropic Hosford−Coulomb fracture initiation model: Theory and application [J]. Engineering Fracture Mechanics, 2015, 147: 480−497.

[17] THOMESEN S, HOPPERSTAD O S, MYHR O R, BØRVIK T. Influence of stress state on plastic flow and ductile fracture of three 6000-series aluminium alloys [J]. Materials Science and Engineering A, 2020, 783: 139295.

[18] PINEAU A, BENZERGA A A, PARDOEN T. Failure of metals I: Brittle and ductile fracture [J]. Acta Materialia, 2016, 107: 424−483.

[19] ZHANG C S, ZHANG Z G, LIU M F, BAO E C, CHEN L, ZHAO G Q. Effects of single- and multi-stage solid solution treatments on microstructure and properties of as-extruded AA7055 helical profile [J]. Transactions of Nonferrous Metals Society of China, 2021, 31(7): 1885−1901.

[20] PENG Guo-sheng, CHEN Kang-hua, CHEN Song-yi, FANG Hua-chan. Evolution of the second phase particles during the heating-up process of solution treatment of Al−Zn−Mg−Cu alloy [J]. Materials Science and Engineering A, 2015, 641: 237−241.

[21] ABDI M, SHABESTARI S G. Novel high strength Al−10.5Si−3.4Cu−0.2Mg alloy produced through two-stage solution heat treatment [J]. Transactions of Nonferrous Metals Society of China, 2021, 31(3): 576−585.

[22] LIU Yong, ZHU Bin, WANG Yi-lin, LI Shi-qi, ZHANG Yi-sheng. Fast solution heat treatment of high strength aluminum alloy sheets in radiant heating furnace during hot stamping [J]. International Journal of Lightweight Materials and Manufacture, 2020, 3(1): 20−25.

[23] MAENO T, MORI K, YACHI R. Hot stamping of high-strength aluminium alloy aircraft parts using quick heating [J]. CIRP Annals, 2017, 66(1): 269−272.

[24] DICK C P, KORKOLIS Y P. Anisotropy of thin-walled tubes by a new method of combined tension and shear loading [J]. International Journal of Plasticity, 2015, 71: 87−112.

[25] DUNAND M, MAERTENS A P, LUO Meng, MOHR D. Experiments and modeling of anisotropic aluminum extrusions under multi-axial loading—Part I. Plasticity [J]. International Journal of Plasticity, 2012, 36: 34−49.

[26] BARLAT F, BREM J C, YOON J W, CHUNG K, DICK R E, LEGE D J, POURBOGHRAT F, CHOI S H, CHU E. Plane stress yield function for aluminum alloy sheets—Part 1. Theory [J]. International Journal of Plasticity, 2003, 19(9): 1297−1319.

[27] ARETZ H. Applications of a new plane stress yield function to orthotropic steel and aluminium sheet metals [J]. Modelling and Simulation in Materials Science and Engineering, 2004, 12(3): 491−509.

[28] ROTH C C, FRAS T, MOHR D. Dynamic perforation of lightweight armor: Temperature-dependent plasticity and fracture of aluminum 7020-T6 [J]. Mechanics of Materials, 2020, 149: 103537.

[29] YAO Di, CAI Li-xun, BAO Chen. A new fracture criterion for ductile materials based on a finite element aided testing method [J]. Materials Science and Engineering A, 2016, 673: 633−647.

[30] LOU Yan-shan, YOON J W, HUH H. Modeling of shear ductile fracture considering a changeable cut-off value for stress triaxiality [J]. International Journal of Plasticity, 2014, 54: 56−80.

[31] WANG Zi-jian, XIANG Chong-chen, ZHANG Yi-sheng. Investigation into constitutive and fracture modeling of hot stamped parts with multiphase [J]. Mechanics of Advanced Materials and Structures, 2021, 29: 1−13.

固溶处理时间对 7075 铝合金热冲压板材塑性及韧性断裂的影响

耿会程 [1]，王义林 [1]，朱 彬 [1]，王子健 [2]，张宜生 [1]

1. 华中科技大学 材料成形与模具技术国家重点实验室，武汉 430074；
2. 苏州大学 沙钢钢铁学院，苏州 215006

摘 要：研究固溶处理时间对 7075 铝合金热冲压板材塑性及韧性断裂的影响。对采用不同固溶处理时间的热冲压试样进行拉伸实验，并采用数字图像相关分析方法获取实验过程中试样的应变。基于实验及仿真，对 Yld2000-3d 屈服准则及 DF2014 断裂模型进行校准，并将其分别用于描述材料的各向异性及断裂行为。同时，对材料的显微组织进行研究。实验及仿真结果表明，热冲压后，7075 铝合金仍残留明显各向异性，且延长固溶处理时间不能有效减弱材料的各向异性。但是，采用较长的固溶时间会提高材料的断裂应变，断裂性能的提高与延长固溶处理时间后第二相颗粒尺寸减小有关。

关键词：7075 铝合金；热冲压；固溶处理时间；各向异性；韧性断裂

(Edited by Bing YANG)